

Semi-Automated Segmentation of Geoscientific Data Using Superpixels

Conrad Koziol
Computational Geosciences
Vancouver, Canada
conrad@compgeoinc.com

Eldad Haber
The University of British Columbia
Vancouver, Canada
ehaber@eoas.ubc.ca

Abstract

Geological processes determine the distribution of resources such as critical minerals, water, and geothermal energy. However, direct observation of geology is often prevented by surface cover such as overburden or vegetation. In such cases, remote and in-situ surveys are frequently conducted to collect physical measurements of the earth indicative of the geology. Developing a geological segmentation based on these measurements is challenging since individual datasets can differ in properties (e.g. units, dynamic ranges, textures) and because the data does not uniquely constrain the geology. Further, as the number of datasets grows the information to constrain geology increases while simultaneously becoming harder to make sense of. Inspired by the concept of superpixels, we propose a deep-learning based approach to segment rasterized survey data into regions with similar characteristics. We demonstrate its use for semi-automated geoscientific mapping with datasets arising from independent sensors and with diverse properties. In addition, we introduce a new loss function for superpixels including a novel regularization parameter penalizing image segmentation with non-connected component superpixels. This improves integration of prior knowledge by allowing better control over the number of superpixels generated.

1. Introduction

Understanding the geology of a domain is one of the fundamental tasks in the earth sciences. Geological processes are a controlling factor in the earth’s evolution, and determine the distribution of resources such as critical minerals, groundwater hydrology, and geothermal energy. However, geology often cannot be observed directly due to the presence of overburden or vegetation. As an alternative, physical properties of the earth indicative of the geology will frequently be measured by conducting remote surveys such as magnetic, gravity, and airborne electromagnetic. This data is often interpreted with a sparse set of geological observations in an expert-driven process manually delineating a geological map. The basic premise of this interpretation is that different geological units have different physical properties and therefore, geophysical observations at scale depend on the geology.

Geological features are not uniquely determined by survey data. This is because the data reflects a certain physical property rather than a geological process. Therefore, an expert-judgement is relied on

for interpretation. This has parallels to medical imaging where radiologists interpret medical images, and contrasts with classic computer vision problems, where grayscale or RGB data is sufficient for instance segmentation. A spectrum of realizations of a geological map can be equally valid, with a subjective selection of a singular output. In many cases it is impossible to know which interpretation is more feasible which makes computerized learning the task of geological segmentation difficult.

Multiple heterogeneous data sources containing independent information are often integrated in geological mapping. Data sources include geophysical surveys, geochemical soil sampling, radiometrics, and hyperspectral imagery. Because data sources measure independent physical properties, images appear visually distinct and can have significantly different features. Increasing numbers of data layers provides better information to constrain geology while simultaneously becoming harder to make sense of.

In this paper, we consider the problem of automated segmentation of a geological domain using rasterized survey data. Inspired by the concept of superpixels, we aim to divide the domain into regions with similar geological characteristics. We advance on previous efforts by taking a deep-learning approach and considering datasets derived from independent sensors with measurements of disparate characteristics. Further, we introduce a new regularization function to facilitate human-in-the-loop control over the number of superpixels generated by soft-superpixel assignment methods.

We approach the problem as an single-shot unsupervised learning image segmentation problem. Our main contributions are:

- Demonstrate the use of superpixels for semi-automating geoscientific mapping
- Propose a new loss function for superpixel mapping, including a novel regularization function penalizing non-connected component superpixels.

The rest of the paper is organized as follows. In Sec. 2 we explore related work and discuss the differences between our work to other known techniques. In Sec. 3 we describe the superpixel method and its training on data. In Sec. 4 we demonstrate the utility of our methodology by an application to the Yalgın Craton in Western Australia and we summarize the paper in Sec. 5.

2. Related Works

Previous applications of superpixels for geological understanding on a regional scale have focused on spectral imagery. Superpixel segmentation of hyperspectral imagery has been used to determine mineral spectra end members [8, 23] and to select bands for lithological discrimination [22]. The work presented in [24] develop a semi-automated tool for lithological boundary detection in optical images based on user input and an iterative algorithm merging superpixels. An automated approach to lithological segmentation of optical images is developed in [19] based on merging independent segmentations from simple linear iterative clustering (SLIC) [2] and a convolutional neural network (CNN).

Numerous image segmentation algorithms have been applied to geological data for detecting structures, lithological units, and alteration [20]. Terracing was an early method used to delineate structures in potential field data [6, 17]. CNNs have been applied to predict preliminary geological form airborne magnetic data [5], spectral imagery [12, 19], and geochemical data [26]. Notably, self-organizing maps with k-means clustering has been used by [3, 4] to predict geological units from multiple geophysical datasets.

This work to our knowledge is the first to propose using superpixels to segment a set of geoscientific datasets. In contrast to previous superpixel applications in the geosciences, which focus on spectral images, we consider data from multiple sensors. The data considered not only have different units and ranges, but are independent of each other, and do not have the same qualitative features (e.g. patterns, textures, edges). In this context superpixels can be thought of as a method for data fusion. By demonstrating that superpixels are an effective tool for segmentation, we provide an alternative approach to self-organizing maps with k-means clustering based on modern deep-learning.

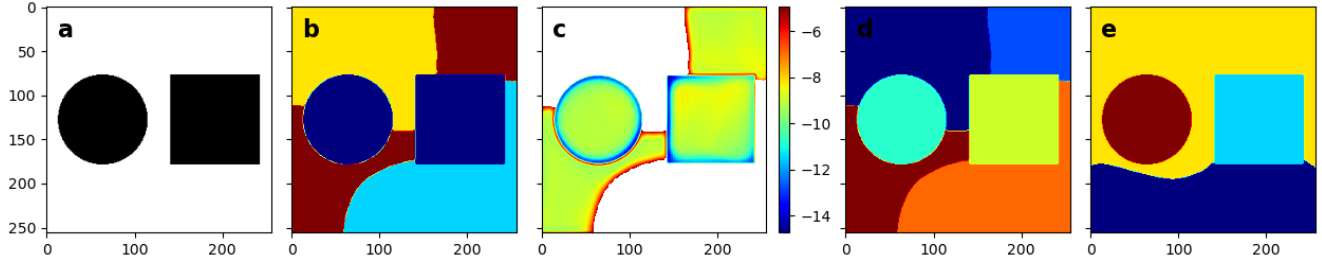


Figure 1. The impact of \mathbf{R}_{cc} demonstrated on a toy problem. a) Toy dataset with background values of zero and foreground values of 1. b) Image segmentation (\mathbf{S}) with four output channels (N) and the coefficient of \mathbf{R}_{cc} set to zero. Notice that the segmentation is discontinuous. Both the circle and square are assigned to the same segment, as are the segments in the top right and bottom left corners. c) $-\|\nabla \mathbf{R}_{cc}\|_2$ pixelwise with respect to the logits. d) Superpixel segmentation (\mathbf{S}') of the output shown in panel (b). Notice there are 6 superpixels. e) Image segmentation leveraging \mathbf{R}_{cc} . Note that segments are continuous, and the number of superpixels corresponds to the number of output channels.

3. Methods

We take an unsupervised single-shot image-segmentation approach to generating superpixels. The description of our methodology follows in three parts. We begin with a preliminary section introducing key notation and standard post-processing applied to neural network outputs to generate superpixels. Next we discuss the core of our methodology which is the objective function we minimize. Finally we detail the neural network architecture and training procedure we use.

3.1. Preliminaries

The input image is denoted by $\mathbf{I} \in \mathbb{R}^{C \times H \times W}$, where C is the number of channels, H is the height of the image, and W is the width of the image. The height and width of the image correspond to the spatial discretization of the domain, while the number of channels corresponds to the available datasets. In our context datasets can be rather different, such as having different physical units and corresponding to different physical properties.

The neural network is specified as $f(\mathbf{I}, \theta) : \mathbb{R}^{C \times H \times W} \times \mathbb{R}^n \rightarrow \mathbb{R}^{N \times H \times W}$, where N is the target number of superpixels. Note that each superpixel is treated as a different channel or class. The output of the neural network is used to generate two probabilistic pixelwise image segmentations. These appear in the objective function and motivated further in that context:

$$\mathbf{P} = \text{softmax}_n(f(\mathbf{I}, \theta)) \quad (1)$$

$$\mathbf{P}^s = \text{sparsemax}_n(f(\mathbf{I}, \theta)) \quad (2)$$

where $\mathbf{P} \in \mathbb{R}^{N \times H \times W}$, $\mathbf{P}^s \in \mathbb{R}^{N \times H \times W}$, and the indices n, i, j are over the N, H, W dimensions respectively. The $\text{sparsemax}_n(\cdot)$ operator is analogous to the softmax function but able to output sparse probabilities [14]. It's defined as the euclidean projection of the input vector onto the probability simplex:

$$\text{sparsemax}(\mathbf{z}) := \operatorname{argmin}_{\mathbf{p} \in \Delta^{K-1}} \|\mathbf{p} - \mathbf{z}\|^2 \quad (3)$$

where Δ^{K-1} is the $(K-1)$ -dimensional probability simplex. Additionally, the neural network output is used to calculate an image segmentation $\mathbf{S} \in \{0, 1, \dots, N-1\}^{H \times W}$ consisting of N classes:

$$\mathbf{S} = \operatorname{argmax}_n (f(\mathbf{I}, \theta)) \quad (4)$$

\mathbf{S} is precursor to the superpixel map since there is no constraint that the image segments are continuous. Spatially independent regions within the image can be assigned the same classification, and hence are not superpixels by definition. This is akin to the difference between semantic and instance segmentation.

Following [2, 7, 21] we postprocess our superpixel segmentation to enforce pixel connectivity (using code available in SciPy [25]). The primary aim of separating spatially discontinuous segments is achieved via a connected component algorithm. Additionally, segments can be either merged or split to enforce superpixel minimum and maximum size constraints. We denote this postprocessed image as $\mathbf{S}' \in \mathbb{R}^{H \times W}$, which is our image superpixel segmentation.

\mathbf{S}' can be used to construct the following superpixelated representation of an image, which useful for visualizing single datalayers and RGB images:

$$\mathbf{I}_{ij}^h = \sum_n \mathbf{1}_n(\mathbf{S}'_{ij}) \frac{\sum_{ij} \mathbf{1}_n(\mathbf{S}'_{ij}) \mathbf{I}_{ij}}{\sum_{ij} \mathbf{1}_n(\mathbf{S}'_{ij})} \quad (5)$$

The image \mathbf{I}^h visualizes each superpixel with an average colour value over all individual pixels within the superpixel.

3.2. Optimization Problem

The core of our superpixel methodology is minimizing the following objective function:

$$\begin{aligned} J(\mathbf{I}, \theta) = & c_1 \sum_n \left(\sum_{ij} \|(\mathbf{c}_n^s - \mathbf{I}_{nij}) \mathbf{P}_{nij}^s\|_2^2 \right) + \\ & c_2 \sum_{ij} \frac{1}{2} \|\nabla \mathbf{P}_{ij}^s\|_2^2 + c_3 \mathbf{R}_{clust}(\mathbf{P}) + c_4 \mathbf{R}_{cc}(\mathbf{P}) \end{aligned} \quad (6)$$

where $\mathbf{c}_n^s = \frac{\sum_{ij} \mathbf{P}_{nij}^s \mathbf{I}_{nij}}{\sum_{ij} \mathbf{P}_{nij}^s}$ is the average dataset values for an image segment, $\mathbf{R}_{clust}(\mathbf{P})$ and $\mathbf{R}_{cc}(\mathbf{P})$ are regularizers defined below, and $c_1 \rightarrow c_4$ are weighting parameters.

The first term promotes an image segmentation grouping pixels with similar data values. Similarity is measured using the L^2 norm, and is function of the difference between the average dataset values for a segment and pointwise dataset values. Multiplication by \mathbf{P}_n^s weights the similarity by the probability of a pixel being assigned to the image segment, and is a differentiable approximation to integrating over the superpixel domains in \mathbf{S}' . We expect most of the image domain to have a low probability of belonging

to a particular segment. The motivation to use \mathbf{P}^s rather than \mathbf{P} is therefore to use sparsity to attenuate the impact of a large number of low probability points.

The second term penalizes the length of boundaries of image segments, and is motivated as a prior that superpixels should have simple geometries. The term $\nabla \mathbf{P}^s$ identifies locations where the probability of segmentation changes, and is used as a proxy for segment boundaries. We select \mathbf{P}^s since we do not require full support over the segmentation probabilities.

[9] previously define a loss function similar to the first two terms above for image segmentation (but not superpixels), inspired by the well studied Mumford-Shah Functional [15] in computer vision. The two differences with our formulation are that we use \mathbf{P}^s rather than \mathbf{P} , and use an L^2 norm in the second term rather than L^1 norm.

\mathbf{R}_{clust} is introduced in [21] and is based on the concept of regularized information maximization:

$$\mathbf{R}_{clust}(\mathbf{P}) = \frac{1}{HW} \sum_n \sum_{ij} -\mathbf{P}_{nij} \log(\mathbf{P}_{nij}) + \lambda \sum_n \hat{\mathbf{P}}_n \log \hat{\mathbf{P}}_n \quad (7)$$

where $\hat{\mathbf{P}}_n = \frac{1}{HW} \sum_{ij} \mathbf{P}_{nij}$, and λ is a weighting factor. Minimizing the first term decreases the entropy of the pixelwise probability distribution of superpixel assignment, while minimizing the second term encourages a similar number of pixels to be assigned to each superpixel.

We introduce a new regularization term applicable to instance-segmentation type problems that penalizes spatial discontinuity. \mathbf{R}_{cc} promotes image segments forming a single connected component in line with the definition of superpixels. When a one-to-one correspondence between image segments and superpixels exists to the first two terms in the objective function (Eq. (6)) are calculated over individual superpixels rather than over arbitrary combinations.

A practical benefit of this regularization term is to provide the user finer control over the number of superpixels. The number of superpixels can be made to be approximately the number of output channels (N). Without this term, the number of superpixels can be far greater than the number of image segments. Fig. 1 demonstrates the impact of \mathbf{R}_{cc} on a toy example.

\mathbf{R}_{cc} is defined as:

$$\mathbf{R}_{cc} = \sum_n 1(\Omega_n^r \neq \emptyset) \left(\sum_{ij \in \Omega_n^r} p_{ij} - \sum_{ij \in \Omega_n^d} \log p_{ij} \right) \quad (8)$$

where Ω_n is the region segmented by the n^{th} superpixel (i.e. $1(\mathbf{S} = n)$), Ω_n^d is the largest connected component of that region, and $\Omega_n^r = \Omega_n - \Omega_n^d$ is the remaining area outside of the largest connected component. An algorithmic implementation of \mathbf{R}_{cc} is shown in Algorithm 1.

At the core of \mathbf{R}_{cc} is a non-differentiable connected component algorithm. We use this to determine the segments which split into multiple connected components. For each such segment, the dominant connected component is identified as having the greatest number of pixels. The pixel locations of the dominant superpixel are one region ($m_{attr} \in [0, 1]^{N \times H \times W}$ in Algorithm 1). The remaining non-dominant pixels are grouped into another ($m_{aver} \in [0, 1]^{N \times H \times W}$ in Algorithm 1). The regularizer is a sum of terms which repels the non-dominant segmented areas away from their current classification and decreases the

Algorithm 1 Connected Component Regularization

```
procedure  $R_{cc}(f \leftarrow f(\mathbf{I}, \theta))$ 
   $p \leftarrow \text{softmax}(f)$ 
   $s \leftarrow \text{argmax}_n(f)$ 
   $c \leftarrow \text{connected\_components}(s)$ 
   $m_{avers}, m_{attr} \leftarrow \text{zeros\_like}(f)$ 
  for  $n$  in  $\text{unique}(s)$  do
     $v \leftarrow c[s = n]$ 
    if  $\text{length}(\text{unique}(v)) > 1$  then
       $a, b \leftarrow \text{unique}(v, \text{return\_counts})$ 
       $a \leftarrow a[\text{argsort}(b, \text{descending})]$ 
       $m_{aver}[n, :, :] \leftarrow (s = n) \text{ and } (cc \neq a[0])$ 
       $m_{attr}[n, :, :] \leftarrow (s = n) \text{ and } (cc = a[0])$ 
    end if
  end for
  return  $\text{mean}(m_{aver}p - m_{attr} \log(p))$ 
end procedure
```

cross-entropy of dominant regions. The regularizer only impacts segmentations which do not form a single connected component. We find the regularizer to be relatively insensitive to the precise function of p used (e.g. p vs $\log p$).

3.3. Implementation

We use a UNet architecture [18] for our neural network $f(\mathbf{I}, \theta)$, on the basis of its effectiveness for segmentation problems and ability to scale with image dimensions. Individual blocks in the UNet are composed of sequences of convolution, ReLU, and Instance Norm. We fix the number of downsampling and upsampling blocks to four, with the number of channels increasing to 64 in the opening block and doubling with each block to reach a maximum of 512 in the bottleneck. Code is written using the PyTorch framework [16].

Based on experimentation, we find Adam [10] with a learning rate of 1e-2 an effective optimizer. We found objective function weighting parameters of $c_1 = 1, c_2 = 1\text{e-}4, c_3 = 100, c_4 = 50$, and $\lambda = 2$ to produce good results, but vary parameters on the basis of the problem. Input images are normalized layerwise, and each dimension is resized to the nearest multiple of 16 to allow four downsampling operations in the UNet.

4. Experiments

We apply superpixel methodology to a 256 km by 256 km domain located in the Yalgın Craton region in Western Australia (Fig. 2). Three data layers available in this region relevant to mineral prospectivity mapping are used for superpixel generation: gravity (Complete Bouguer Anomaly [11]), magnetic (Total Magnetic Intensity [1]), and tau (Time Constant from Airborne Electromagnetic Surveys [13]). Each datalayer is gridded at 500 m resolution, and has dimensions of 512x512 pixels. We apply quantile normalization to the mag data due to its high dynamic range. In addition, we standardize all layers before inputting to the neural network.

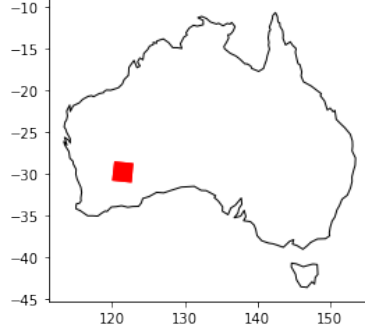


Figure 2. Location of study domain in Australia. Coordinates in WGS84.

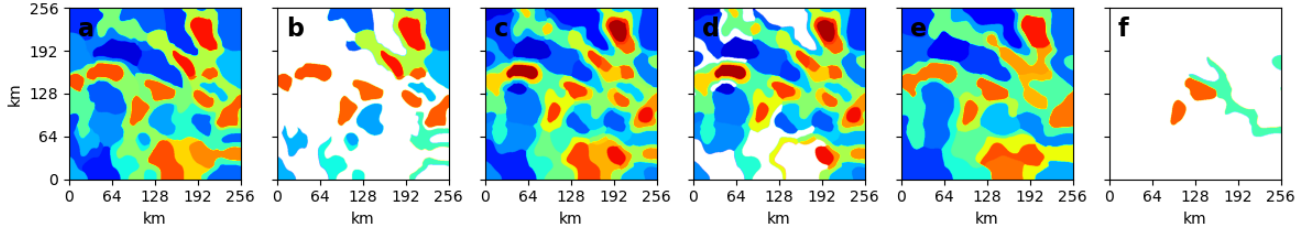


Figure 3. The impact of \mathbf{R}_{cc} demonstrated on the tau dataset. Panels display representation of the dataset (\mathbf{I}^h) created using pre-supapixel image segmentations \mathbf{S} a) Using code from [7]. b) Visualization in (a) but masking single connected component segments. c) Our code without \mathbf{R}_{cc} . d) Analogous to (b). e) Our code with \mathbf{R}_{cc} . e) Analogous to (b). Observe there are far fewer non-contiguous segments and that they cover significantly less of the domain.

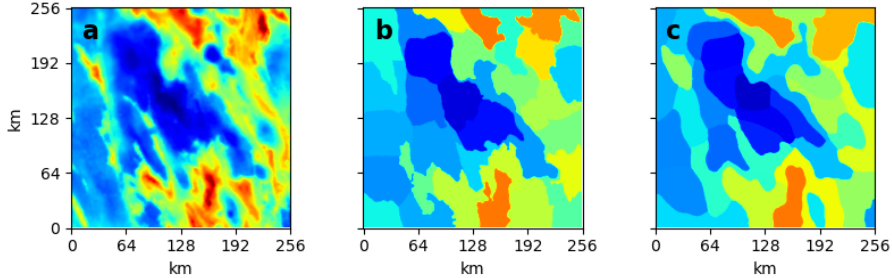


Figure 4. Superpixel segmentation applied to gravity data. a) gravity data. b) SLIC superpixel image (\mathbf{I}^h). c) Our method superpixel image (\mathbf{I}^h).

As a first step, we demonstrate the impact of \mathbf{R}_{cc} by generating a superpixel representation of the tau dataset with two unsupervised deep learning approaches: our method and that of [7]. We set the number of output channels (logits) for the networks to be 35. Results are plotted (Fig. 3) before post-processing enforcing connectivity (i.e. \mathbf{S}). The output of the methodology of [7] and our methodology without \mathbf{R}_{cc} leads to 53 and 83 connected components respectively. Neglecting postprocessing, these would be the number of superpixels. Adding \mathbf{R}_{cc} to our model decreases the number of connected components to 34.

\mathbf{R}_{cc} allows user-control over the number of superpixels generated. It's effect is to penalize image

segments representing multiple superpixels, pushing the system to have no more than N superpixels. The ability to constrain the number of superpixels is essential when the number of superpixels is selected based on prior knowledge such physical characteristics of the system, downstream task requirements, or user preference.

We also contrast superpixels (Fig. 4) based on the tau data using both our unsupervised deep learning approach and SLIC. Due to the numerous parameter choices in each model and subjectivity of the problem, the choice of algorithm can viewed as part of the modelling process. However, the advantages of deep learning are that it works in feature space rather than in data space, incorporates nonlinearities into the loss-function, and integrates information across the entire image. Experiments show better qualitative superpixel segmentation using our methodology than SLIC.

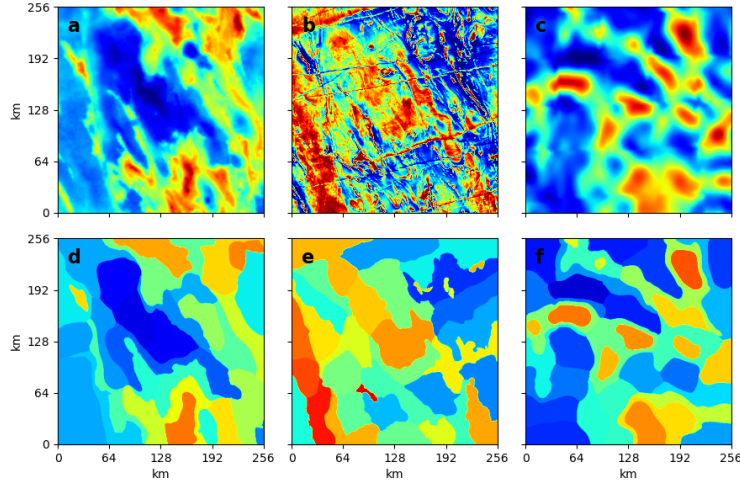


Figure 5. Superpixel segmentation applied to individual data layers. Columns correspond to gravity, magnetic, and tau data. Target of 35 superpixels per dataset, with realized values of 32, 35, and 39 respectively. a-c) Data d-f) Corresponding map of super pixel representation (\mathbf{I}^h).

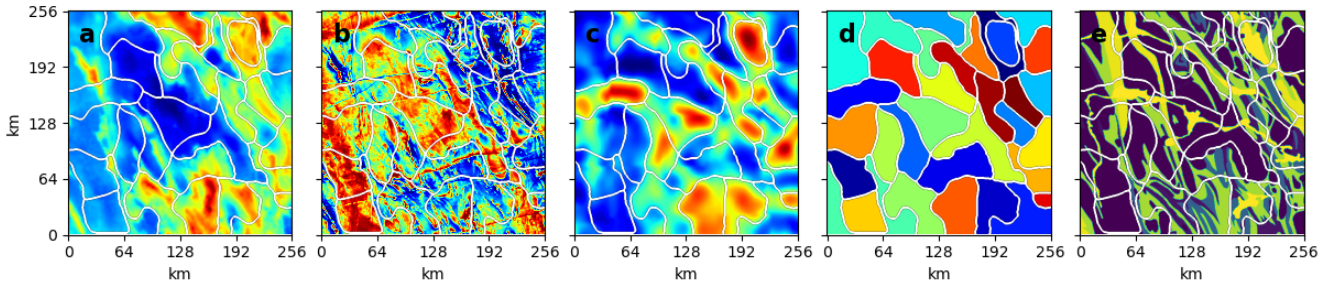


Figure 6. Superpixel segmentation applied to the combination of gravity, magnetic, and tau data layers. (c.f. image with superpixel segmentation applied layer-wise). Targeted and realized number of superpixels is 35 and 33. a-c) Individual gravity, mag, tau layers with combined segmentation overlaid on top. d) Superpixels with random color assignment and outlines in white. e) Superpixels overlaid onto geological map.

Superpixel segmentation (Fig. 5) is applied independently to gravity, magnetic, and tau datasets in our study domain. Qualitatively we observe good results, with the individual segmentations reflecting the

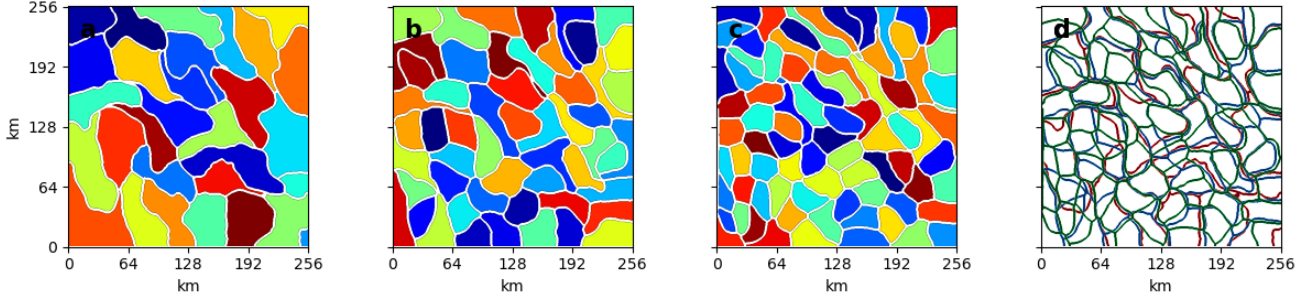


Figure 7. Three superpixel segmentations of the combined magnetic, gravity, and tau datalayers. The target (realized) number of superpixels are a) 30 (30). b) 60 (54). c) 90 (83). Panel d) shows all three segmentations overlaid with the colours red, blue, green corresponding to panels (a), (b), and (c) respectively.

patterns in the data. The best correspondence between the superpixelated image and the original dataset is for the tau image, which has the smoothest features. However, our segmentation performs well for the highly textured magnetic image. Low frequency features are broadly captured (Fig. 5b), with some high frequency features being retained.

We observe little correlation between the superpixel segmentations, which is unsurprising based on the observation that the images look different and that these datasets provide approximately independent geoscientific information. These provide a baseline for comparison with respect to holistic superpixel generation.

Next we proceed with segmenting the study domain based on all three datasets (Fig. 6). We observe that superpixels are generally coherent across all the datasets, although instances where the delineation of a superpixel is arbitrary for a particular layer. Although the aim of superpixels is not to recreate a geological map (nor is it necessarily possible), we compare the superpixel map to a geological map of the region for completeness.

Superpixel segmentation is amenable to a human-in-the-loop workflow. Fig. 7 shows the results of three different superpixel segmentations applied to the combination of the datalayers with increasing numbers of superpixels. Numerous places exhibit consistent boundaries. This indicates that where the model is well constrained the output is similar, while showing the adaptability to display different solutions where the segmentation may be more complex.

5. Conclusion

We present a superpixel approach for fusing geoscientific data into a representative spatial segmentation. This provides an objective, semi-automated method for segmenting a domain into regions with similar physical characteristics. Further, we formulate a new loss function for superpixels, including a novel regularization parameter based on connected-components that allows user-control over the number of superpixels generated.

The method we present is complementary to expert judgement, and in practice can provide a baseline result to be interpreted or modified in the context of aggregate information. Additionally, different solutions can be quantitatively compared using the loss function and parameter choices can be transferred across spatial domains. By handling an arbitrary number of input layers our methodology can be leveraged in cases where qualitative understanding is most difficult.

While we demonstrate our methodology with an application to geophysical data motivated by mineral

exploration, it is applicable across a spectrum of geospatial datasets and use-cases. A natural extension beyond the continuous raster data we consider would be to incorporate point data and layers with partial coverage.

References

- [1] *Geophysical Acquisition & Processing Section 2020. Magnetic Anomaly Map of Australia, Seventh Edition, 2019 TMI Greyscale image.* Geoscience Australia, Canberra, 2020. <http://pid.geoscience.gov.au/dataset/ga/144733>. 6
- [2] Radhakrishna Achanta, Appu Shaji, Kevin Smith, Aurelien Lucchi, Pascal Fua, and Sabine Süsstrunk. Slic superpixels compared to state-of-the-art superpixel methods. *IEEE transactions on pattern analysis and machine intelligence*, 34(11):2274–2282, 2012. 2, 4
- [3] Cleyton de Carvalho Carneiro, Stephen James Fraser, Alvaro Penteadó Crósta, Adalene Moreira Silva, and Carlos Eduardo de Mesquita Barros. Semiautomated geologic mapping using self-organizing maps and airborne geophysics in the brazilian amazon. *Geophysics*, 77(4):K17–K24, 2012. 2
- [4] Angela Carter-McAuslan and Colin Farquharson. Predictive geologic mapping from geophysical data using self-organizing maps: A case study from baie verte, newfoundland, canada. *Geophysics*, 86(4):B249–B264, 2021. 2
- [5] Matthieu Cedou, Erwan Gloaguen, Martin Blouin, Antoine Caté, Jean-Philippe Paiement, and Shiva Tirdad. Preliminary geological mapping with convolution neural network using statistical data augmentation on a 3d model. *Computers & Geosciences*, 167:105187, 2022. 2
- [6] Lindrith Cordell and Anne E McCafferty. A terracing operator for physical property mapping with potential field data. *Geophysics*, 54(5):621–634, 1989. 2
- [7] Moshe Eliasof, Nir Ben Zikri, and Eran Treister. Rethinking unsupervised neural superpixel segmentation. In *2022 IEEE International Conference on Image Processing (ICIP)*, pages 3500–3504. IEEE, 2022. 4, 7
- [8] Martha S Gilmore, David R Thompson, Laura J Anderson, Nader Karamzadeh, Lukas Mandrake, and Rebecca Castaño. Superpixel segmentation for analysis of hyperspectral data sets, with application to compact reconnaissance imaging spectrometer for mars data, moon mineralogy mapper data, and ariadnes chaos, mars. *Journal of Geophysical Research: Planets*, 116(E7), 2011. 2
- [9] Boah Kim and Jong Chul Ye. Mumford–shah loss functional for image segmentation with deep learning. *IEEE Transactions on Image Processing*, 29:1856–1866, 2019. 5
- [10] Diederik P Kingma and Jimmy Ba. Adam: A method for stochastic optimization. *arXiv preprint arXiv:1412.6980*, 2014. 6
- [11] R.J.L. Lane, P.E. Wynne, Y. Poudjom Djomani, W.R. Stratford, J.A. Barretto, and F. Caratori Tontini. *2019 Australian National Gravity Grids: Free Air Anomaly, Complete Bouguer Anomaly, De-trended Global Isostatic Residual, 400 m cell size (includes Point Located Data)*. Geoscience Australia, 2020. 6
- [12] Rasim Latifovic, Darren Pouliot, and Janet Campbell. Assessment of convolution neural networks for surficial geology mapping in the south rae geological region, northwest territories, canada. *Remote sensing*, 10(2):307, 2018. 2
- [13] Yuseyn LeyCooper. *AusAEM WA 2020-21, Eastern Goldfields & East Yilgarn Airborne Electromagnetic Survey Blocks TEMPEST® airborne electromagnetic data and GALEI conductivity estimates*. Geoscience Australia, Canberra, 2021. <http://pid.geoscience.gov.au/dataset/ga/144621>. 6
- [14] Andre Martins and Ramon Astudillo. From softmax to sparsemax: A sparse model of attention and multi-label classification. In *International conference on machine learning*, pages 1614–1623. PMLR, 2016. 4

- [15] David Bryant Mumford and Jayant Shah. Optimal approximations by piecewise smooth functions and associated variational problems. *Communications on pure and applied mathematics*, 1989. 5
- [16] Adam Paszke, Sam Gross, Francisco Massa, Adam Lerer, James Bradbury, Gregory Chanan, Trevor Killeen, Zeming Lin, Natalia Gimelshein, Luca Antiga, et al. Pytorch: An imperative style, high-performance deep learning library. *Advances in neural information processing systems*, 32, 2019. 6
- [17] Jeffrey D Phillips. Terrace; a terracing procedure for gridded data, with fortran programs, and vax command procedure, unix c-shell, and dos batch file implementations. Technical report, US Geological Survey: Books and Open-File Reports Section [distributor], 1992. 2
- [18] Olaf Ronneberger, Philipp Fischer, and Thomas Brox. U-net: Convolutional networks for biomedical image segmentation. In *International Conference on Medical image computing and computer-assisted intervention*, pages 234–241. Springer, 2015. 6
- [19] Xuejia Sang, Linfu Xue, Xiangjin Ran, Xiaoshun Li, Jiwen Liu, and Zeyu Liu. Intelligent high-resolution geological mapping based on slic-cnn. *ISPRS International Journal of Geo-Information*, 9(2):99, 2020. 2
- [20] Hojat Shirmard, Ehsan Farahbakhsh, R Dietmar Müller, and Rohitash Chandra. A review of machine learning in processing remote sensing data for mineral exploration. *Remote Sensing of Environment*, 268:112750, 2022. 2
- [21] Teppei Suzuki. Superpixel segmentation via convolutional neural networks with regularized information maximization. In *ICASSP 2020-2020 IEEE International Conference on Acoustics, Speech and Signal Processing (ICASSP)*, pages 2573–2577. IEEE, 2020. 4, 5
- [22] Yulei Tan, Laijun Lu, Lorenzo Bruzzone, Renchu Guan, Zhiyong Chang, and Chen Yang. Hyperspectral band selection for lithologic discrimination and geological mapping. *IEEE Journal of Selected Topics in Applied Earth Observations and Remote Sensing*, 13:471–486, 2020. 2
- [23] David R Thompson, Lukas Mandrake, Martha S Gilmore, and Rebecca Castano. Superpixel endmember detection. *IEEE Transactions on Geoscience and Remote Sensing*, 48(11):4023–4033, 2010. 2
- [24] Yathunanthan Vasuki, Eun-Jung Holden, Peter Kovesi, and Steven Micklethwaite. An interactive image segmentation method for lithological boundary detection: A rapid mapping tool for geologists. *Computers & Geosciences*, 100:27–40, 2017. 2
- [25] Pauli Virtanen, Ralf Gommers, Travis E. Oliphant, Matt Haberland, Tyler Reddy, David Cournapeau, Evgeni Burovski, Pearu Peterson, Warren Weckesser, Jonathan Bright, Stéfan J. van der Walt, Matthew Brett, Joshua Wilson, K. Jarrod Millman, Nikolay Mayorov, Andrew R. J. Nelson, Eric Jones, Robert Kern, Eric Larson, C J Carey, İlhan Polat, Yu Feng, Eric W. Moore, Jake VanderPlas, Denis Laxalde, Josef Perktold, Robert Cimrman, Ian Henriksen, E. A. Quintero, Charles R. Harris, Anne M. Archibald, Antônio H. Ribeiro, Fabian Pedregosa, Paul van Mulbregt, and SciPy 1.0 Contributors. SciPy 1.0: Fundamental Algorithms for Scientific Computing in Python. *Nature Methods*, 17:261–272, 2020. 4
- [26] Ziye Wang, Renguang Zuo, and Fanfan Yang. Geological mapping using direct sampling and a convolutional neural network based on geochemical survey data. *Mathematical Geosciences*, pages 1–24, 2022. 2